

A β -barrel for oil transport through lipid membranes: Dynamic NMR structures of AlkL

Tobias Schubeis^a, Tanguy Le Marchand^a, Csaba Daday^b, Wojciech Kopec^b, Kumar Tekwani Movellan^c, Jan Stanek^{a,1}, Tom S. Schwarzer^d, Kathrin Castiglione^{d,2}, Bert L. de Groot^b, Guido Pintacuda^{a,3}, and Loren B. Andreas^{a,c,3}

^aCentre de Résonance Magnétique Nucléaire à Très Hauts Champs de Lyon (FRE 2034–CNRS, Université Claude Bernard Lyon 1, École Normale Supérieure Lyon), Université de Lyon, 69100 Villeurbanne, France; ^bBiomolecular Dynamics Group, Max Planck Institute for Biophysical Chemistry, 37077 Göttingen, Germany; ^cDepartment for NMR-based Structural Biology, Max Planck Institute for Biophysical Chemistry, 37077 Göttingen, Germany; and ^dInstitute of Biochemical Engineering, Technical University of Munich, 85748 Garching, Germany

Edited by David Baker, University of Washington, Seattle, WA, and approved July 22, 2020 (received for review February 14, 2020)

The protein AlkL is known to increase permeability of the outer membrane of bacteria for hydrophobic molecules, yet the mechanism of transport has not been determined. Differing crystal and NMR structures of homologous proteins resulted in a controversy regarding the degree of structure and the role of long extracellular loops. Here we solve this controversy by determining the de novo NMR structure in near-native lipid bilayers, and by accessing structural dynamics relevant to hydrophobic substrate permeation through molecular-dynamics simulations and by characteristic NMR relaxation parameters. Dynamic lateral exit sites large enough to accommodate substrates such as carvone or octane occur through restructuring of a barrel extension formed by the extracellular loops.

membrane protein | lipid bilayers | protein structure | protein dynamics | magic-angle spinning

As in any cell, the outer membrane of bacteria is composed of a lipid bilayer that separates intracellular processes from the outside environment. In addition to this lipid bilayer, Gram-negative bacteria have evolved an outer leaflet composed mainly of lipopolysaccharides (LPS) (1). While the inner membrane is permeable to hydrophobic molecules, the charged and densely packed LPS layer reduces their permeation rates 50–100-fold, as compared with phospholipid membranes (2–4) (Fig. 1). Since these membrane properties limit uptake of nutrients, bacteria make use of a wide array of passive transmembrane porins, β -barrels of sufficiently large diameter to allow nonspecific permeation of small molecules (1, 5).

The OmpW family of outer-membrane proteins (6), classified as porins, is widespread in Gram-negative bacteria. These proteins fold into eight-stranded β -barrels displaying a narrow pore diameter in the membrane, which appears too compact to permit passage of even small molecular substrates. Yet there is mounting evidence that the OmpW family protein AlkL functions as a passive importer of hydrophobic molecules. AlkL is found on the same operon together with genes necessary for oxidation of alkanes and utilization as a carbon and energy source (7) (Fig. 1). These include an alkane monooxygenase (AlkB) and associated rubredoxin (AlkG) and rubredoxin reductase (AlkT), as well as an aldehyde dehydrogenase (AlkH) and alcohol dehydrogenase (AlkK) and a positive regulatory protein (AlkS). Due to its location on the *alk* operon, AlkL was proposed to have a passive transport function, increasing the rate of diffusion for alkanes. Definitive evidence for such transport was recently found by incorporating the alkane hydroxylase complex of *Pseudomonas putida* GPo1 with and without AlkL in cells (8–10), and in even more defined nanoreactor polymersomes (11). These studies demonstrate transport of alkanes, and a cyclic methyl ketone, respectively, in line with the wide substrate utilization of *P. putida*. In polymersomes, the increase in transport-dependent production of product alcohol occurs with an increase in the number of incorporated AlkL molecules.

While the transport function of AlkL has been established, a controversy in the transport mechanism still exists. By analogy to other β -barrels (12–15), a lateral exit was proposed based on X-ray structures of OmpW (16) and OprG (17), formed from proline residues that break the hydrogen bonding at the end of the transmembrane β -strands. The X-ray structure reveals a β -barrel arrangement in the loops; however, the 1.3-Å radius of the putative lateral opening is incompatible with the size of known substrates of AlkL such as alkanes or monocyclic molecules. The static X-ray structures are therefore insufficient to explain the mode of action, and a view complemented by dynamics is needed (18–20). In contrast, micellar solution NMR structures lack the putative exit sites entirely, and rather display flexible extracellular loops (21, 22). This supports an alternative vision of transport characterized by hinge motions of the loops and major rearrangements of backbone segments or partial loss of secondary structure. Here we solve this controversy by determining the de novo NMR structure in near-native lipid bilayers for AlkL, and by detecting structural dynamics relevant to

Significance

Here we show how AlkL, a minimalistic outer-membrane protein from oil-consuming bacteria, exploits dynamics of extracellular loops to channel substrate across the polysaccharide barrier and into the hydrophobic interior of the outer membrane. This work represents a unique example of a side-by-side atomic-level structure determination by solution NMR in detergents and by solid-state NMR in lipid bilayers, which critically demonstrates the importance of a lipid environment to investigate function. Corroborating our experimental measurements, molecular-dynamics simulations capture substrate transit via lateral openings. The capacity to unravel membrane protein function under near-native conditions, fueled by the latest method developments, opens up a new frontier for their investigation, and provides thereby for improved fundamental insights into biological processes.

Author contributions: T.S., B.L.d.G., G.P., and L.B.A. designed research; T.S., T.L.M., C.D., W.K., K.T.M., J.S., and L.B.A. performed research; T.S. and K.C. contributed new reagents/analytic tools; T.S., T.L.M., C.D., W.K., K.T.M., J.S., and L.B.A. analyzed data; and T.S., B.L.d.G., G.P., and L.B.A. wrote the paper.

The authors declare no competing interest.

This article is a PNAS Direct Submission.

This open access article is distributed under Creative Commons Attribution-NonCommercial-NoDerivatives License 4.0 (CC BY-NC-ND).

¹Present address: Faculty of Chemistry, University of Warsaw, 02089 Warsaw, Poland.

²Present address: Chemical and Biological Engineering, Institute of Bioprocess Engineering, Friedrich-Alexander-Universität Erlangen-Nürnberg, 91052 Erlangen, Germany.

³To whom correspondence may be addressed. Email: Guido.Pintacuda@ens-lyon.fr or land@nmr.mpiibpc.mpg.de.

This article contains supporting information online at <https://www.pnas.org/lookup/suppl/doi:10.1073/pnas.2002598117/-DCSupplemental>.

First published August 19, 2020.

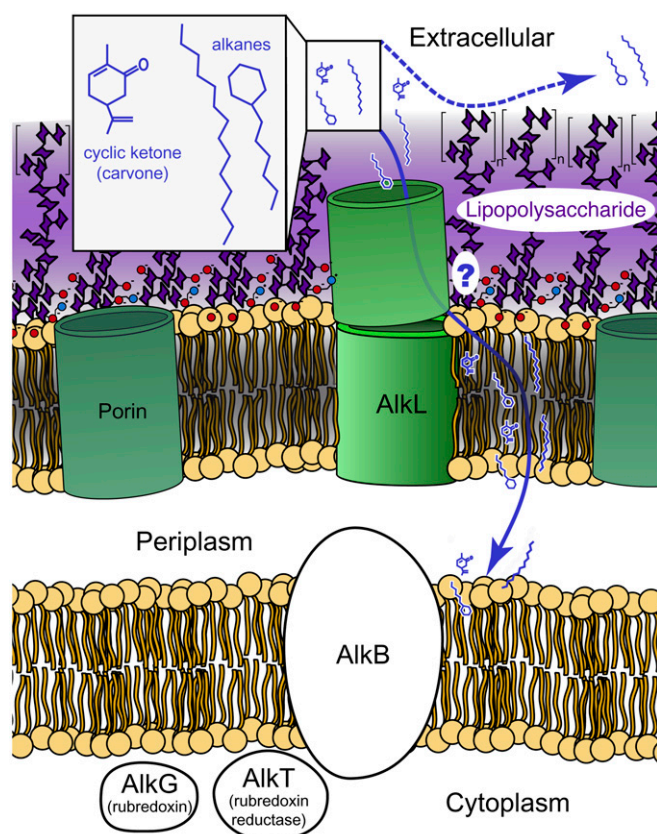


Fig. 1. The main features of the inner and outer membranes of Gram-negative bacteria, and location of key proteins of the Alk operon. Hydrophobic molecules such as alkanes and terpenoids (*Inset*, blue), do not readily traverse (blue dashed arrow) the LPS (purple). Instead, their permeation is assisted by porins such as AlkL (green). A permeation path through the extracellular loops with a lateral exit into the hydrophobic bilayer (blue arrow) was proposed based on crystal structures of AlkL homologs (8). Detergent micelle solution data support a more dynamic process without a specific lateral release (21, 22).

hydrophobic substrate permeation through molecular-dynamics (MD) simulations and by characteristic NMR relaxation parameters. The data revealed a dynamic lateral exit mechanism that involves continuous restructuring of the barrel extension and release into the lipid bilayer through ephemeral openings.

Results and Discussion

To understand the mechanism of the transport function of AlkL, we determined two separate structures, one in detergent micelles by using well-established solution NMR protocols and a second in lipid bilayers, by using the latest magic-angle spinning (MAS) NMR methodology. This is complemented by characterization of structural dynamics by both simulation and NMR relaxation measurements. The solution NMR data were acquired from octyl glucoside solution (OG), with traces of the refolding detergent LDAO using a perdeuterated AlkL sample. Both of these detergents are considered mild. Lipid-embedded AlkL data were acquired from 1,2-dimyristoyl-*sn*-glycero-3-phosphocholine (DMPC) bilayer samples, as well as from preparations reconstituted in the presence of LPS, using both fully protonated as well as perdeuterated AlkL. In these latter preparations, negative stain transmission electron micrographs reveal the presence of liposomes, without detectable protein aggregates (*SI Appendix*, Fig. S1). Furthermore, NMR experiments probing protein-to-lipid interactions

demonstrate that AlkL is in immediate contact with lipids (23). Residues all across the β -barrel show contact with the lipid acyl chains, defining the transmembrane region of the protein (*SI Appendix*, Fig. S2). For sensitivity reasons, the lipid-to-protein ratio (LPR) was minimized to 0.5 by mass (~ 18 by mole). The resulting spectrum at LPR of 0.5 is unchanged from an LPR of 10, but spectral quality degrades with LPR of 0.25 (*SI Appendix*, Fig. S3). This combined evidence shows that AlkL is properly embedded in the membrane and that the protein structure is independent of concentration over the range detectable by MAS NMR.

NMR Structures. Two structures were determined from assigned resonances in 170 out of 203 residues in lipids, and 132 residues in detergent. Unassigned signals in lipids belong mainly to the flexible *N*-terminus, to periplasmic turns, and to short portions of the first extracellular loop, and are absent from many of the NMR spectra. In detergent, only the first loop was assigned, and displays chemical shifts characteristic of unstructured proteins. Approximately 50 additional unassigned signals in the 2D ^1H - ^{15}N heteronuclear single quantum coherence fall in the same chemical shift range, indicating a lack of β -structure also for the remaining loops. This is in contrast to the DMPC preparation where assignments in all loops indicate structure. No nuclear Overhauser effect (NOE) transfer to these peaks was observed, also pointing to lack of structure. Yet additional evidence pointing toward random coiled loops in detergents was obtained by preparing a sample in D_2O . In D_2O only the assigned residues of the transmembrane region remained detectable, indicating protection from HD exchange. In an MSP1 nanodisc preparation (*SI Appendix*, Fig. S4) without detergent, mainly unassigned residues appeared, indicating that the rigid transmembrane domain is not detectable in the larger nanodisc particle. Consistent with the DMPC preparation where more loop residues are structured, some peaks that were flexible in detergent are not detected in the nanodisc preparation.

Structures were calculated from a clear pattern of proton-proton cross-strand contacts in radio-frequency-driven recoupling (RFDR) or NOE spectra. While traditional three-dimensional (3D) HHN- and HNN NOE spectroscopy (NOESY) spectra provided sufficient resolution in solution, we turned to four-dimensional (4D) HNNH-RFDR spectra in solids to remove ambiguities in the assignment of cross-strand restraints (*SI Appendix*, Figs. S5 and S6). The fully protonated sample together with >100 -kHz MAS (24) granted access to sidechain resonance assignments and collection of sidechain-to-sidechain distance restraints which was used to refine the bilayer-bound structure. All restraints used for calculation of the two structures are listed in *SI Appendix*, Table S2.

The two AlkL structures determined by MAS and solution NMR are shown in Fig. 2 *A* and *B*, and share an identical transmembrane (TM) β -barrel motif. The lipid-embedded structure, however, reveals an elongated β -barrel fold, extending into the region where polysaccharide would be in LPS, similar to homologous crystal structures. Structured loop residues also occur in a sample reconstituted in the presence of LPS and DMPC lipids (*SI Appendix*, Fig. S7) as indicated by the detection of the same loop resonances in cross-polarization-based spectra. Only minor chemical shift perturbation (CSP) is observed. Conversely, the loops are highly flexible in OG detergent micelles, which is in turn consistent with previous determinations of homologs by solution NMR. That the bilayer-embedded structure in this case appears closer to homology models of crystal structures is in contrast to a recent solid-state NMR structure of OmpG (25) obtained in 2D crystalline lipid bilayers, which agreed better with the solution NMR conformation. In the case of AlkL, the perturbation due to

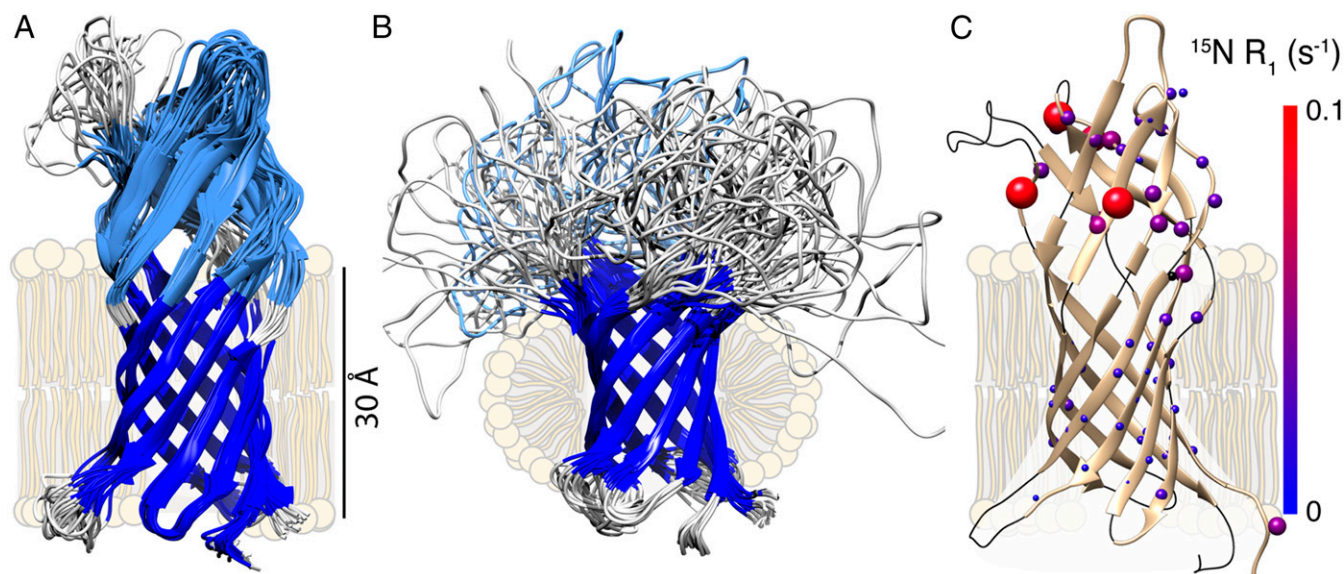


Fig. 2. NMR structure and dynamics of AlkL. The structural ensembles in lipids and in detergent are depicted in *A* and *B*, respectively. Loops (that form a barrel extension in *A*) are colored in light blue where residues are assigned, and in gray where no assignment could be made. Temperatures were 305 K for the lipid bilayer sample and 308 K for the detergent-solubilized sample. In *C*, ^{15}N R_1 rates in lipids are indicated on the lowest-energy conformer of the protein structure in *A*.

detergent micelles appears to outweigh the influence of crystal contacts.

Site-specific ^{15}N longitudinal relaxation (R_1) (26) in the lipid-embedded sample explains the apparent inconsistency between the two models in lipids and in micelles, by assessing dynamic motions occurring on a fast (nanosecond) timescale (Fig. 2*C* and *SI Appendix*, Table S3). While the TM region displays uniform low relaxation rates, the extracellular portion is subject to enhanced *ns* backbone dynamics. These measurements define a clear junction in flexibility between the TM and extracellular regions of the structure. Considering that transport through the AlkL inner pore would require channel opening, the low R_1 relaxation rates of the TM region are in favor of a model where the TM region is serving solely as an anchor for the more flexible extracellular part. This complements the rigid representation of extracellular β -strands in Fig. 2*A*, and is consistent with the fact that a detergent environment (Fig. 2*B*) results in loss of structure in the loops. The same mobility that is likely needed to allow for the transport function of the protein appears to predispose the extracellular part to destabilization by even mild detergent, an effect which likely plagues other membrane proteins (27).

Since the lipid bilayer most closely mimics the native membrane, and these conditions support a folded extracellular domain, we focused on the membrane-embedded sample and solid-state NMR for further structural and dynamical analysis of transport in AlkL. The surface hydrophobicity of the bilayer NMR structure (Fig. 3*A*) demonstrates the expected hydrophobic exterior (tan) in the transmembrane region, with polar and charged residues lining the interior. Reverse polarity (purple) is seen on the extracellular barrel extension, which has a hydrophilic exterior.

These structural features define a long, accessible hydrophobic pore, leading up to the membrane interfacial region. Within the TM domain, the pore narrows to less than the radius of a water molecule as visualized using HOLE (28) (Fig. 3*B*), which along with a hydrophilic character suggests lateral release into the hydrophobic membrane rather than continued transport through

the protein. A cross-sectional view (Fig. 3*D*) reveals the tight stacking of long internal sidechains that block diffusion of molecules through the TM region. At the same time, the structure features six small openings, two of which (I and IV) are located close to the membrane surface (Fig. 3*C*), in the vicinity of several proline residues that break the pattern of cross-strand hydrogen bonds. Site I is the most prominent in our NMR structure, while site IV corresponds to the previously proposed putative lateral exit (8, 16, 17). These potential exit sites would require dynamic rearrangement to accommodate the size of substrate. Detailed views of the hydrophobic residues lining the extracellular pore are displayed in Fig. 3*D* and *E*. The residue R168 is shown occluding the pore at the top of the TM barrel, and in the same view, the residues V75 and T54 are seen near the mouth of the largest potential exit site I/II.

Dynamical Lateral Release Model. The validity of this “dynamical lateral release” model is supported by MD simulations (Figs. 4 and 5) and NMR relaxation rates sensitive to slow motions (Fig. 6), recorded both in the presence and the absence of the substrates octane and carvone. *P. putida* utilizes a wide substrate range including linear alkanes, cyclic hydrocarbons, and even polycyclic molecules (PAHs) (7). The alkanes are metabolized by the alk proteins, whereas PAHs are utilized by additional metabolic pathways, making octane an ideal molecule to investigate the transport function of AlkL. All simulations were initiated in explicit water from the solid-state NMR structure of AlkL embedded in a membrane. Simulations in LPS membrane (details in the *SI Appendix*) were initiated with 1-palmitoyl-2-oleoyl-*sn*-glycero-3-phosphocholine on the inner leaflet (Fig. 4). These MD simulations conform to the expected behavior of the LPS, namely, that the hydrophobic octane does not traverse the barrier characterized by polar sugar moieties functionalized with charged phosphate groups. As expected, octane enters the hydrophobic pore formed by loop residues, and traverses this region of the protein up until the level of the lipid head groups. At this point, the pore is occluded by charged sidechains, in particular R168. Fig. 4*A* and *B* shows two snapshots from the MD

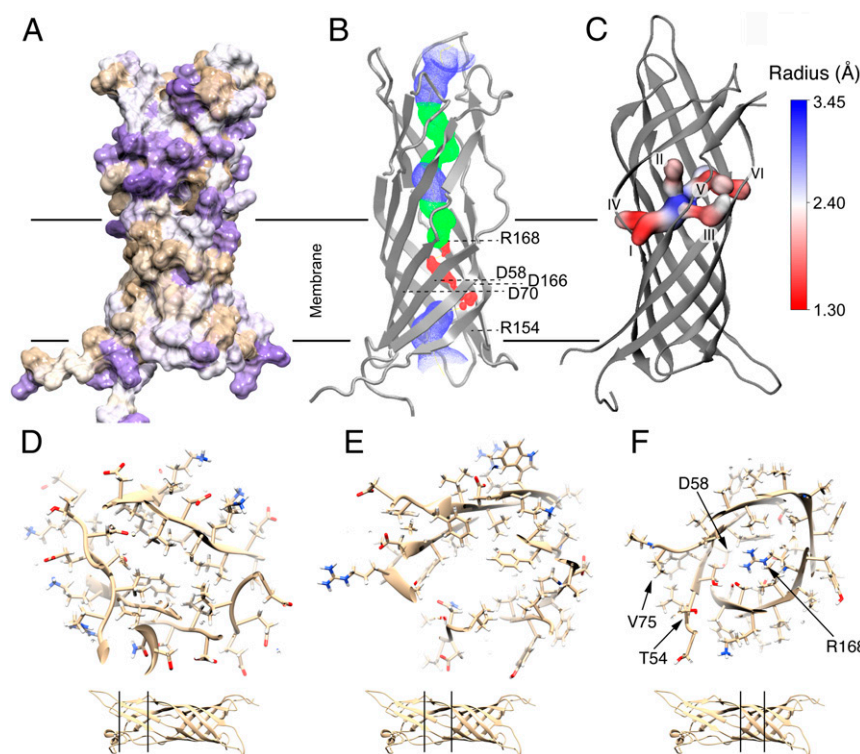


Fig. 3. The bilayer structure of AlkL, and potential exit. **A** shows surface hydrophobicity (tan) and hydrophilicity (purple). In **B**, the central pore is visualized using the HOLE (18) program. Red indicates a diameter less than one water molecule (1.15 Å), while green and blue indicate a radius of one water (1.15–2.30 Å), and more than one water molecule (>2.30 Å), respectively. The positions of charged residues constraining the interior are labeled. In **C**, potential lateral exit sites are visualized. In **D–F**, slices through the β -barrel extension are characterized by a hydrophobic inner surface (**D** and **E**), with the central pore blocked by arginine in the membrane-embedded part of the protein **F**. In the same vicinity, a lateral opening occurs near residues T54 and V75.

trajectory, as well as a comparison of the bilayer penetration depth of octane in LPS alone and mediated by AlkL (Fig. 4A, *Inset*). This comparison was made with the zero depth referenced to the LPS phosphate groups. Consistent with the low rate (millisecond timescale) of transport that supports growth of yeast and *E. coli* on sugar (29–31), these 1 μ s MD trajectories were not able to capture substrate permeation events, even when reinitialized from structures where octane was already bound in the pore. Nonetheless, the protein did readily allow deep penetration of substrate into the membrane, and we were able to observe full octane transit in MD trajectories in a simplified DMPC environment. Fig. 4C–E shows several snapshots from 1- μ s trajectories in which octane escaped into the lipid membrane from three different interstrand locations, namely sites I and IV identified in Fig. 3C as well as between P147 and P171. While the LPS appears to stabilize the protein, increasing the energy barrier for such events, the events may nevertheless represent permeation pathways albeit that occur much more slowly in the native membrane.

In addition to octane, we observed permeation for the monocyclic ketone carvone, which is an intermediate-sized oil that provides a challenging test of the transport function of AlkL. Carvone has a similar structure to a cyclic methyl ketone used to demonstrate accelerated transport facilitated by AlkL (11). Fig. 5A shows the initial conformation of AlkL embedded into a DMPC membrane in explicit water. The simulations in DMPC match the conditions of the NMR structure determination, where the protein was properly folded. Over multiple microsecond trajectories, the structure is stable, and the barrel extension exhibits higher plasticity than the transmembrane region, in agreement with the experimental data. Within 100 ns, carvone molecules

cluster onto the barrel extension and several molecules are seen to concurrently occupy the pore (Fig. 5B). After 1,000 ns, all carvone molecules have diffused into the membrane or remain within the barrel extension (Fig. 5C). Although this simulation time was again not sufficient to observe lateral release of carvone, release did occur in further simulations, initialized from structures where carvone was already bound in the pore (see *SI Appendix, Figs. S8 and S9* for the detailed simulation protocols). As visualized by four snapshots in Fig. 5D, carvone is observed to exit toward the membrane uniquely through site I. This shows that exit of both octane, and the larger carvone molecule is possible without a pair of proline residues breaking cross-strand hydrogen bonds, and therefore represents a distinct class of lateral exit site. The simulations in DMPC do not preserve the barrier properties of LPS. They can therefore not be used to assess AlkL-mediated acceleration of permeation, but can be used to probe the permeation pathway. As expected, most carvone molecules enter the membrane directly in DMPC, and relatively few carvone molecules enter the membrane via AlkL. This nevertheless demonstrates the transport function of the protein. Since there is no active transport in AlkL, we expect nearly all octane or carvone to partition to the hydrophobic membrane, and this is indeed observed in long enough MD simulations. In a living system, consumption of the substrate occurs via AlkB in the inner membrane, necessitating exit from the inner leaflet of the outer membrane, and entry into the inner membrane lipids. To our knowledge, these phospholipid membranes do not present a substantial barrier to AlkB substrates, and no additional proteins have been identified in the passive flux of metabolites once through the LPS barrier.

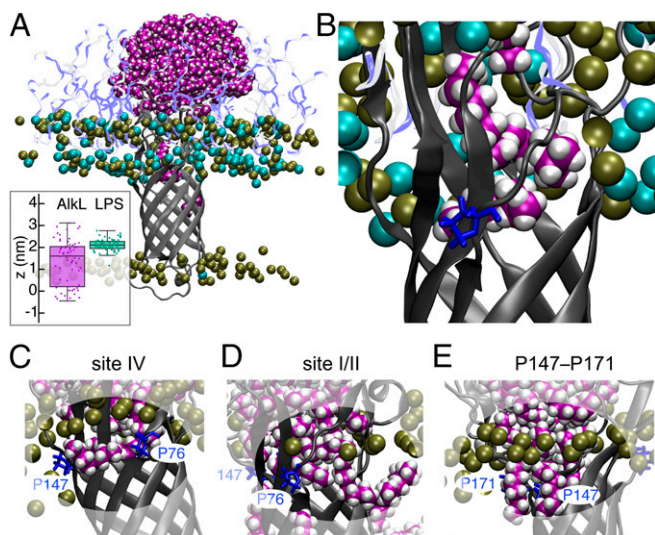


Fig. 4. MD simulations of AlkL in LPS (A and B) and in DMPC (C–E) with the substrate octane. Octane enters the protein and reaches near the depth (z) of the acyl lipid chains (A, *Inset*). A “prerelease” snapshot of octane in LPS is shown in B. Three different octane release locations were observed in DMPC lipids, at the site IV proposed in homologs (C), through the new site I/II (D), and through the prolines P147 and 171 (E), on the opposite side of the barrel. LPS sugars are displayed in purple, phosphate in dark green, calcium in cyan, and the protein in gray. Octane is shown in purple and white spheres.

Transit events through AlkL are made possible by dynamic remodeling of the pore, as evidenced by the distinct distributions of conformers in the absence and presence of carvone (Fig. 5 E and F). Notably, the main conformers identified in simulations with bound carvone (Fig. 5E) mostly retained a widened potential exit site I, as compared to the NMR structure (Fig. 3C). Furthermore, there is hardly any overlap in the phase-space regions explored by the protein without and with bound carvone (Fig. 5F). Interestingly, the NMR structure is located in between these two regions. The motion along the first (largest) eigenvector in a principal component analysis (PCA) shows that the difference without and with bound carvone is related to the opening of the newly identified site I for carvone permeation (Movie S1).

We used two further NMR measurements to detect structural variations and motional processes relevant to hydrophobic substrate permeation: chemical shift perturbations (CSPs) and ^{15}N longitudinal relaxation under RF spin lock ($R_{1\rho}$) (Fig. 6 and SI Appendix, Table S3). High CSPs highlight significant changes in the barrel extension for both carvone and octane. Of particular interest are large CSP values in residues flanking P76, which lies in a β -bulge separating sites I and IV. Coincident with large CSPs are enhanced values of ^{15}N $R_{1\rho}$ (Fig. 6C), an indicator of transient chemical shift changes (exchange phenomena) and microsecond–millisecond motions. $R_{1\rho}$ rates were also sensitive to the presence of carvone in the barrel extension (SI Appendix, Fig. S10). Overall, the NMR data are direct signatures of the transient expansion of the pore captured by MD simulations, providing a connection between loop flexibility and permeation. Of the sites implicated by dynamics measurements, sites III–VI are flanked by β -strands with a well-defined hydrogen bonding pattern in lipids (SI Appendix, Fig. S11), indicating a more static structure. Only the site I/II is larger and adjacent to the highly flexible loop 1. It is no surprise that this location supports dynamic release of the larger carvone molecule.

Whether the dynamic lateral release mechanism described here is general for proteins of the OmpW family remains an open question. While for AlkL, there is no evidence for hydrophilic substrates, and indeed no CSP was observed in AlkL with leucine as substrate (SI Appendix, Fig. S12), amino acids have been proposed for homologous proteins. If an OmpW family protein does accommodate hydrophilic substrates, lateral transport may represent the first part of the mechanism, which would traverse the polysaccharide barrier of the outer membrane. Complete traversal would then require transmembrane passage through the aliphatic lipid tails, which presents a barrier to hydrophilic substrate. This might occur via oligomeric interfaces or partner proteins. For example, crystal packing interactions are found in OmpW crystals (Protein Data Bank [PDB] ID code 2F1V) in a region corresponding to the exit site in AlkL (SI Appendix, Fig. S11), and a pore large enough for glycine is found in a homology model of OprG based on the OmpW crystal structure (32). Alternatively, OmpW family members might act in concert with other proteins present in the outer membrane in a similar way as a type 9 secretion system that exports protein through a lateral exit to a porin (33). Although no such protein has been identified, the outer membrane is rich with a plethora of membrane proteins that may play a role. Further evidence is needed to understand whether AlkL homologs exhibit the same transport function via a lateral release mechanism as proposed here for AlkL.

Conclusions. Through a combination of NMR and MD simulations, we uncovered a dynamic translocation pathway in an eight-stranded β -barrel for the import of hydrophobic molecules. The side-by-side comparison of sample conditions shows a strong impact of lipids and LPS in particular in stabilizing the protein. This demonstrates that even a β -barrel, often regarded as particularly stable, can be strongly impacted by environmental conditions in the functionally important extracellular loops. The sensitivity to environmental conditions also explains discrepancies related to environmental influences affecting crystal and solution structures. The capacity of NMR to site-specifically probe structure and dynamics of membrane proteins in lipid bilayers was the foundation for these mechanistic insights, and is key to understanding proteins in motion. Here specifically, the transmembrane transport mechanism that is implicated by CSP and MD provides the underpinning for potential future biotechnology and bioengineering applications.

Methods

Sample Preparation. Uniformly ^{13}C , ^{15}N -labeled and ^2H , ^{13}C , ^{15}N -labeled samples of AlkL (28–230) from *P. putida* Gp01 were expressed in *Escherichia coli*, purified, and reconstituted in lipids according to a protocol described previously (34), and recently adapted to accommodate isotopic labeling (35). A full description is provided in SI Appendix, Supplementary Text. Samples in the presence of octane or carvone were prepared in saturated solutions, by addition of a small drop of oil to the surface of the sample buffer. Liposomes were separated by centrifugation before packing in NMR rotors.

NMR Spectroscopy. Solution NMR spectra were recorded at $\omega_{\text{H}}/2\pi = 1$ GHz and 600 MHz on Bruker Avance III instruments equipped with cryogenic probes using ^2H , ^{13}C , ^{15}N -labeled AlkL. Solid-state NMR spectra were recorded at $\omega_{\text{H}}/2\pi = 1$ GHz and 800 MHz, on Bruker Avance III instruments equipped with 0.7- and 1.3-mm HCN probes spinning at MAS rates of 111.111 kHz (^{13}C , ^{15}N -labeled AlkL) or 60 kHz (^2H , ^{13}C , ^{15}N -labeled AlkL). Spectrometer settings, as well as acquisition parameters specific for each 3D and 4D spectrum, and for site-specific ^{15}N R_1 (26) and ($R_{1\rho}$) (36) rates, are discussed in SI Appendix, Supplementary Text and summarized in SI Appendix, Table S1. The spectral quality underlying resonance assignment datasets (37, 38) is demonstrated in the pair of CA-N-H correlation spectra shown in SI Appendix, Fig. S13 and the assignments are discussed in detail in a separate manuscript (39). CSPs induced by the presence of carvone or octane were

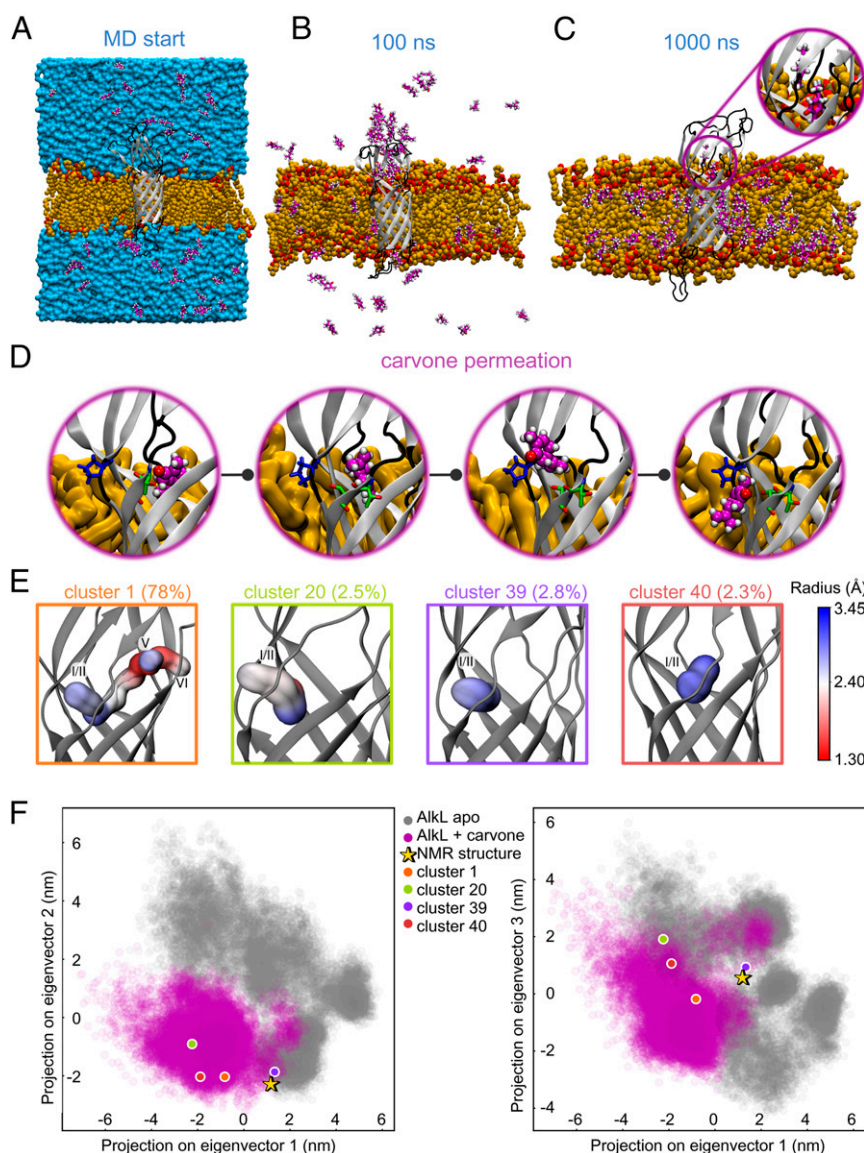


Fig. 5. MD simulations of AlkL in DMPC with and without carvone. A–C show simulation snapshots in which carvone molecules (magenta) spontaneously enter both the membrane (orange) and the protein (gray) from explicit water (blue). D shows a full permeation event, in which one carvone molecule exits the protein through site I/II and emerges near the lipid headgroup. Lining the exit, threonine residues 53, 54 and proline 76 are shown as green and blue sticks, respectively. E shows central structures of main clusters (occurrence % indicated) identified in MD simulations with bound carvone and the lateral exits in each cluster. F shows the projections of simulations into first three eigenvectors obtained through PCA of all MD trajectories.

obtained from (H)CANH and (H)CONH spectra, and were calculated as the RMSD of ^1H , $^{13}\text{C}\alpha$, and ^{15}N shifts, with relative scaling of 1, 0.3, and 0.15, respectively (40).

Solution NMR Structure Calculation. Several unambiguous distance restraints were manually assigned in the well-resolved 3D (H)N(HH)NH spectrum, leading, along with dihedral angle restraints, to an initial model. A set of hydrogen bond restraints was generated for resonances that showed no exchange with D_2O . NOESY peak lists were added for automated assignment and structure calculation using CYANA 3.98 (41). Further details are discussed in *SI Appendix, Supplementary Text*, and calculation statistics are reported in *SI Appendix, Table S2*.

MAS NMR Structure Calculation. Several unambiguous distance restraints were manually assigned in the well-resolved 4D (H)NH(H)NH spectrum leading, along with dihedral angle restraints, to a first model. Hydrogen bond restraints were included where cross-peaks in the 4D spectrum were identified with β -sheet chemical shift, and forming a clear pattern of

contacts expected for antiparallel β -sheets (*SI Appendix, Figs. S3 and S4*). The hydrogen bond restraints are indicated in *SI Appendix, Fig. S11*. RFDR and band-selective spectral spin diffusion-SD (35) peak lists were added for automated assignment and structure calculation using CYANA 3.98 (41). The final structure made use of both backbone and sidechain protons (*SI Appendix, Fig. S14*). Further details are discussed in *SI Appendix, Supplementary Text*, and calculation statistics are reported in *SI Appendix, Table S2*.

Relaxation Data Fitting. Signal intensity decays of both ^{15}N R_1 and $R_{1\rho}$ relaxation experiments were fit to a monoexponential function. Error estimate was performed with Monte Carlo simulations: synthetic datasets are produced by adding Gaussian random noise (with the same SD as the experimental noise) to the backcalculated decay curves. The error was determined as the SD of the ensemble of dynamical parameters obtained by fitting 1,000 synthetic datasets.

MD Simulations. All simulations were performed with GROMACS 2018 simulation software (42). *SI Appendix, Supplementary Text* discusses the details

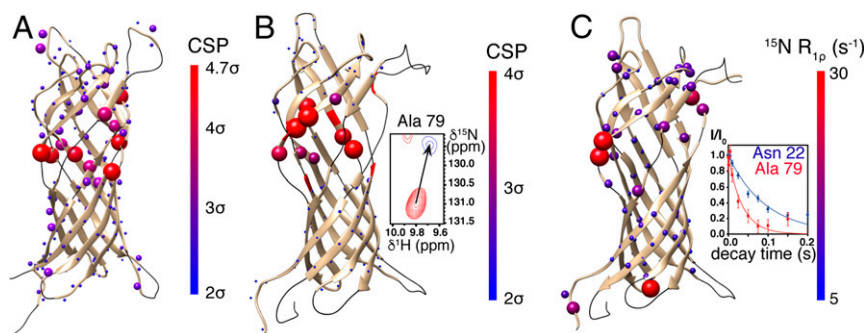


Fig. 6. Mapping the conduction pathway. *A* and *B* show CSP upon addition of the substrates octane and carvone, respectively. *B* (Inset) shows the amide ^{15}N - ^1H correlation peak of Ala-79 before (red lines) and after addition of carvone (blue lines). *C* shows ^{15}N $R_{1\rho}$ relaxation rates, a measure of microsecond-millisecond motions. (Inset) Relaxation curves obtained for a rigid (Asn-22, blue) and a more flexible residue (Ala-79, red) are shown.

of the force fields and parameters used, as well as the procedures for preparing the systems prior to MD simulations. Four systems containing AlkL were simulated for 1,000 ns each ("Alk apo" simulations). After the addition of carvone, four new systems were initially simulated for 1,000 ns each. Further simulations were spawned by monitoring the position of bound carvone and simulated for additional 100 ns in several cycles, as shown in *SI Appendix, Fig. S6*.

Data Availability. The atomic coordinates and restraints were deposited in the Protein Data Bank, <https://www.rcsb.org/> [PDB ID codes 6QWR (43) and 6QAM

(44)], and chemical shifts were deposited in the Biological Magnetic Resonance Data Bank, <http://www.bmrb.wisc.edu/> [ID 34365 (45) and 34338 (46)].

ACKNOWLEDGMENTS. The work was funded by the European Research Council (ERC-2015-CoG GA 648974 to G.P.), the CNRS (IR-RMN FR3050), the European Commission (Project iNext GA 653706), the German Research Foundation (Emmy Noether Program Grant AN1316/1-1 and SFB803 Grant INST 186/794-3 Project B11 to L.B.A.; FOR 2518 "Dynlon," Project P5 to W.K. and B.L.d.G.), and the German Federal Ministry of Education and Research (BMBF GA 031A178 to K.C.). J.S. was supported by MSCA incoming fellowship GA 661799.

1. R. Koebnik, K. P. Locher, P. Van Gelder, Structure and function of bacterial outer membrane proteins: Barrels in a nutshell. *Mol. Microbiol.* **37**, 239–253 (2000).
2. R. R. Chen, Permeability issues in whole-cell bioprocesses and cellular membrane engineering. *Appl. Microbiol. Biotechnol.* **74**, 730–738 (2007).
3. R. E. Hancock, The bacterial outer membrane as a drug barrier. *Trends Microbiol.* **5**, 37–42 (1997).
4. H. Nikaido, Prevention of drug access to bacterial targets: Permeability barriers and active efflux. *Science* **264**, 382–388 (1994).
5. H. Nikaido, Porins and specific channels of bacterial outer membranes. *Mol. Microbiol.* **6**, 435–442 (1992).
6. J. W. Fairman, N. Noinaj, S. K. Buchanan, The structural biology of β -barrel membrane proteins: A summary of recent reports. *Curr. Opin. Struct. Biol.* **21**, 523–531 (2011).
7. J. D. Van Hamme, A. Singh, O. P. Ward, Recent advances in petroleum microbiology. *Microbiol. Mol. Biol. Rev.* **67**, 503–549 (2003).
8. C. Grant *et al.*, Identification and use of an alkane transporter plug-in for applications in biocatalysis and whole-cell biosensing of alkanes. *Sci. Rep.* **4**, 5844 (2014).
9. M. K. Julsing *et al.*, Outer membrane protein AlkL boosts biocatalytic oxygen-functionalization of hydrophobic substrates in *Escherichia coli*. *Appl. Environ. Microbiol.* **78**, 5724–5733 (2012).
10. Y. M. van Nuland, G. Eggink, R. A. Weusthuis, Application of AlkBGT and AlkL from *Pseudomonas putida* GPo1 for selective alkyl ester ω -Oxyfunctionalization in *Escherichia coli*. *Appl. Environ. Microbiol.* **82**, 3801–3807 (2016).
11. T. S. Schwarzer, L. Klermund, G. Wang, K. Castiglione, Membrane functionalization of polymersomes: Alleviating mass transport limitations by integrating multiple selective membrane transporters for the diffusion of chemically diverse molecules. *Nanotechnology* **29**, 44LT01 (2018).
12. H. Dong *et al.*, Structural basis for outer membrane lipopolysaccharide insertion. *Nature* **511**, 52–56 (2014).
13. E. M. Hearn, D. R. Patel, B. W. Lepore, M. Indic, B. van den Berg, Transmembrane passage of hydrophobic compounds through a protein channel wall. *Nature* **458**, 367–370 (2009).
14. S. Qiao, Q. Luo, Y. Zhao, X. C. Zhang, Y. Huang, Structural basis for lipopolysaccharide insertion in the bacterial outer membrane. *Nature* **511**, 108–111 (2014).
15. B. van den Berg, P. N. Black, W. M. Clemons Jr., T. A. Rapoport, Crystal structure of the long-chain fatty acid transporter FadL. *Science* **304**, 1506–1509 (2004).
16. H. Hong, D. R. Patel, L. K. Tamm, B. van den Berg, The outer membrane protein OmpW forms an eight-stranded β -barrel with a hydrophobic channel. *J. Biol. Chem.* **281**, 7568–7577 (2006).
17. D. S. Touw, D. R. Patel, B. van den Berg, The crystal structure of OprG from *Pseudomonas aeruginosa*, a potential channel for transport of hydrophobic molecules across the outer membrane. *PLoS One* **5**, e15016 (2010).
18. K. Oxenoid, J. J. Chou, A functional NMR for membrane proteins: Dynamics, ligand binding, and allosteric modulation. *Protein Sci.* **25**, 959–973 (2016).
19. A. Sekhar, L. E. Kay, An NMR view of protein dynamics in health and disease. *Annu. Rev. Biophys.* **48**, 297–319 (2019).
20. K. Wüthrich, G. Wagner, Internal motion in globular proteins. *Trends Biochem. Sci.* **3**, 227–230 (1978).
21. R. Horst, P. Stanczak, K. Wüthrich, NMR polypeptide backbone conformation of the *E. coli* outer membrane protein W. *Structure* **22**, 1204–1209 (2014).
22. I. Kucharska, P. Seelheim, T. Edrington, B. Liang, L. K. Tamm, OprG harnesses the dynamics of its extracellular loops to transport small amino acids across the outer membrane of *Pseudomonas aeruginosa*. *Structure* **23**, 2234–2245 (2015).
23. E. E. Najbauer *et al.*, Probing membrane protein insertion into lipid bilayers by solid-state NMR. *ChemPhysChem* **20**, 302–310 (2019).
24. L. B. Andreas *et al.*, Structure of fully protonated proteins by proton-detected magic-angle spinning NMR. *Proc. Natl. Acad. Sci. U.S.A.* **113**, 9187–9192 (2016).
25. J. S. Retel *et al.*, Structure of outer membrane protein G in lipid bilayers. *Nat. Commun.* **8**, 2073 (2017).
26. N. Giraud *et al.*, Quantitative analysis of backbone dynamics in a crystalline protein from nitrogen-15 spin-lattice relaxation. *J. Am. Chem. Soc.* **127**, 18190–18201 (2005).
27. C. Chipot *et al.*, Perturbations of native membrane protein structure in alkyl phosphocholine detergents: A critical assessment of NMR and biophysical studies. *Chem. Rev.* **118**, 3559–3607 (2018).
28. O. S. Smart, J. M. Goodfellow, B. A. Wallace, The pore dimensions of gramicidin A. *Biophys. J.* **65**, 2455–2460 (1993).
29. R. J. Naftalin, N. Green, P. Cunningham, Lactose permease H⁺-lactose symporter: Mechanical switch or Brownian ratchet? *Biophys. J.* **92**, 3474–3491 (2007).
30. E. B. Waygood, T. Steeves, Enzyme I of the phosphoenolpyruvate: Sugar phosphotransferase system of *Escherichia coli*. Purification to homogeneity and some properties. *Can. J. Biochem.* **58**, 40–48 (1980).
31. L. Ye, J. A. Berden, K. van Dam, A. L. Kruckeberg, Expression and activity of the Hxt7 high-affinity hexose transporter of *Saccharomyces cerevisiae*. *Yeast* **18**, 1257–1267 (2001).
32. R. R. Sanganna Gari *et al.*, Quaternary structure of the small amino acid transporter OprG from *Pseudomonas aeruginosa*. *J. Biol. Chem.* **293**, 17267–17277 (2018).
33. F. Lauber, J. C. Deme, S. M. Lea, B. C. Berks, Type 9 secretion system structures reveal a new protein transport mechanism. *Nature* **564**, 77–82 (2018).
34. T. S. Schwarzer, M. Hermann, S. Krishnan, F. C. Simmel, K. Castiglione, Preparative refolding of small monomeric outer membrane proteins. *Protein Expr. Purif.* **132**, 171–181 (2017).
35. M. G. Jain *et al.*, Selective ^1H - ^1H distance restraints in fully protonated proteins by very fast magic-angle spinning solid-state NMR. *J. Phys. Chem. Lett.* **8**, 2399–2405 (2017).
36. J. R. Lewandowski, H. J. Sass, S. Grzesiek, M. Blackledge, L. Emsley, Site-specific measurement of slow motions in proteins. *J. Am. Chem. Soc.* **133**, 16762–16765 (2011).

37. E. Barbet-Massin *et al.*, Rapid proton-detected NMR assignment for proteins with fast magic angle spinning. *J. Am. Chem. Soc.* **136**, 12489–12497 (2014).
38. J. Stanek *et al.*, NMR spectroscopic assignment of backbone and side-chain protons in fully protonated proteins: Microcrystals, sedimented assemblies, and amyloid fibrils. *Angew. Chem. Int. Ed. Engl.* **55**, 15504–15509 (2016).
39. T. Schubeis *et al.*, Resonance assignment of the outer membrane protein AlkL in lipid bilayers by proton-detected solid-state NMR. *Biomol. NMR Assign.*, 10.1007/s12104-020-09964-5 (2020).
40. E. A. Chekmenev, J. Paulino, R. Fu, T. A. Cross, “Anisotropic and isotropic chemical shifts perturbations from solid state NMR spectroscopy for structural and functional biology” in *Modern Magnetic Resonance*, G. A. Webb, Ed. (Springer International Publishing, Cham, 2018), pp. 505–519.
41. P. Güntert, L. Buchner, Combined automated NOE assignment and structure calculation with CYANA. *J. Biomol. NMR* **62**, 453–471 (2015).
42. D. Van Der Spoel *et al.*, GROMACS: Fast, flexible, and free. *J. Comput. Chem.* **26**, 1701–1718 (2005).
43. T. Schubeis, L. B. Andreas, G. Pintacuda, Solid-state NMR structure of outer membrane protein AlkL in DMPC lipid bilayers. Protein Data Bank. <https://www.rcsb.org/structure/6qwr>. Deposited 6 March 2019.
44. T. Schubeis, L. B. Andreas, G. Pintacuda, Solution NMR structure of outer membrane protein AlkL. Protein Data Bank. <https://www.rcsb.org/structure/6qam>. Deposited 19 December 2018.
45. T. Schubeis, L. B. Andreas, G. Pintacuda, Solid-state NMR structure of outer membrane protein AlkL in DMPC lipid bilayers. Biological Magnetic Resonance Data Bank. http://www.bmrb.wisc.edu/data_library/summary/index.php?bmrblid=34365. Deposited 6 March 2019.
46. T. Schubeis, L. B. Andreas, G. Pintacuda, Solution NMR structure of outer membrane protein AlkL. Biological Magnetic Resonance Data Bank. http://www.bmrb.wisc.edu/data_library/summary/index.php?bmrblid=34338. Deposited 19 December 2018.